Ga-Doped LLZO Solid-State Electrolyte with Unique "Plate-like" Morphology Derived from Water Hyacinth (*Eichhornia crassipes*) Aquatic Weed: Waste to Wealth Conversion

Kuntal Ghosh and Mir Wasim Raja*

Read Online

ACCESS | Metrics & More | Article Recommendations | SI Supporting Information

ABSTRACT: An attempt has been made for the first time to convert waste biomass such as water hyacinth (WH) to a functional energy material in a cost-effective way. The present research describes a novel exo-templating methodology to develop engineered microstructure of Ga-doped $Li_7La_3Zr_2O_{12}$ ($Li_{6.25}La_3Ga_{0.25}Zr_2O_{12}$, referred as WH-Ga-LLZO) solid-state electrolyte for its use in all solid-state lithium batteries (ASSLBs) by mimicking the intercellular structure of water hyacinth (*Eichhornia crassipes*), an invasive and noxious aquatic plant. The developed exo-templated methodology offers a low calcination

Water Hyacinth (Plant) → Water Hyacinth (Fiber) → Exo-templating → Solid State Electrolyte → Ga-LLZO
Waste to Wealth

temperature of 1000 °C in air where all the major peaks could be indexed as cubic garnet, as confirmed by XRD. The FESEM micrographs revealed a unique "plate-like" morphology that mimicked the intercellular structure of water hyacinth fiber. The bulk lithium-ion conductivity in the WH-Ga-LLZO electrolyte was found to be 3.94×10^{-5} S/cm. Li/WH-Ga-LLZO/Li cells were galvanostatically cycled for a continuous 295 h with increasing step current densities from 28 $\mu A/cm^2$ without a short circuit. The highest current density as measured for maximum polarization in a symmetric cell was found to be 452 $\mu A/cm^2$. The WH exo-templated methodology was thus developed and optimized and can be extended for synthesizing any application-specific multifunctional materials.

INTRODUCTION

It is always fascinating to design application-specific materials with self-assembling architectures, controlled morphology, and a high degree of crystallinity by using templates of geometrically complex biostructures available in nature. In the last two decades, varieties of biotemplates, such as bacteria,[1,2] eggshell membranes,[3] paper,[4] insect wings,[5] cotton,[6−8] algae,[9] fruits,[10] etc., have been used to synthesize metals, alloys, metal oxides, semiconductors, ceramics, and composite materials. These templates or bioscaffolds offer plenty of room to engineer material structures same as the template's morphology. Depending on their nature of synthesis, Ozin et al.[11] proposed that biotemplating methods may be classified in three broad categories, that is, the negative template method, positive template method, and surface step edge template method. Among them, exo-templating offers an easy synthesis option where the bioscaffold is used as a sacrificial template and is removed at the end of the synthesis process, resulting in an exo-pattern of the template used. Several researchers worldwide reported hierarchically ordered structures using bio-templates of different natures and types. Chen et al. reported the synthesis of $SrCrO_4$ nanostructures with excellent optical properties by mimicking an inner squama layer of onion.[12] In 2014, Song et al.[7] successfully synthesized $LaFeO_3$ hollow fibers from cotton with enhanced gas-sensing properties. TiO_2

crystals derived from the eggshell membrane by Kale et al.[4] showed a unique morphology and interesting properties when tested in dye-sensitized solar cells. Zhang et al.[10] successfully used grapefruit exocarp as a template for the synthesis of porous hierarchical biomorphic SnO_2 crystalline materials with an average particle size of ∼10 nm. Wang et al.[13] used butterfly wings to synthesize quasi-periodic structures of Titania photoanodes. In the recent past, we also successfully synthesized a $BaBi_{0.2}Co_{0.35}Fe_{0.45}O_{3-\delta}$ (BBCF) perovskite-type oxygen separation membrane with a "nanorod" microstructure using water hyacinth (*Eichhornia crassipes*; *E. crassipes*) as an exo-template and obtained a twofold increase in electronic conductivity compared to the conventionally prepared BBCF materials.[14]

In the present work, an attempt has been made for the first time to develop a unique "plate-like" microstructure by mimicking the intercellular structure of WH fibers. Here, we particularly emphasizes a facile synthesis process of preparing a
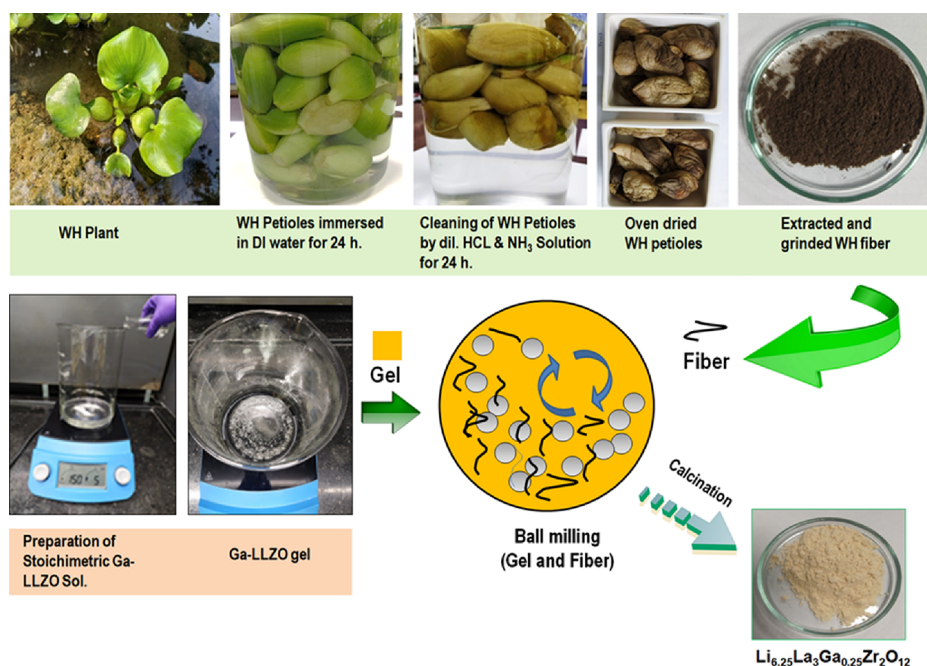
Figure 1. Steps involved in the synthesis process of Ga-doped LLZO powder.

gallium-doped $Li_7La_3Zr_2O_{12}$-based ($Li_{6.25}La_3Ga_{0.25}Zr_2O_{12}$, henceforth will be referred as WH-Ga-LLZO) garnet solid-state electrolyte for its application in all solid-state lithium batteries (ASSLBs) using water hyacinth (*E. Crassipes*) as a sacrificial biotemplate. In 2007, Murugan et al.[15] first proposed $Li_7La_3Zr_2O_{12}$ (LLZO) garnet in its cubic polymorph with fast lithium-ion conductivity ($10^{-3}-10^{-4}$ S/cm) at room temperature. Since then, the LLZO-based garnet material emerged as one of the most promising candidate for next-generation solid-state electrolytes for lithium batteries. However, the stability of the cubic phase of LLZO could only be achieved by high-temperature solid-state sintering, which may invite a loss of lithium in the stoichiometry and appearance of unwanted impurities.[16] To overcome the stability issues in LLZO cubic garnet partial substitutions by Ta^{5+}, Nb^{5+}, Te^{6+}, and W^{6+} at Zr^{4+} sites, Al^{3+} and Ga^{3+} in Li sub-lattices were proposed.[17−22] Among them, Ga doping reported to be effective in order to both stabilize the cubic LLZO phase and provide fast lithium ion mobility originating from Coulombic repulsion between Ga^{3+} and Li^+ ions.[23] In another approach, attempts were also made to prepare pristine/doped LLZO cubic phases at a lower temperature by using wet chemical methods such as conventional sol−gel,[24] pechini,[25] co-precipitation,[26] glycine combustion,[27] etc.

Here, we are reporting for the first time a novel synthesis methodology of a Ga-doped LLZO-based garnet electrolyte material using water hyacinth, an aquatic weed, as an exo-template. In India, the impact of water hyacinth is much higher in aquatic ecosystems and waterways than that of other parts of the globe because of Indian climate conditions, which help in the accelerated growth of this invasive species. Water hyacinth chokes the aquatic ecosystem by producing a non-penetrative mat over the freshwater bodies that prevents sunlight, which results into a smooth breeding ground for mosquitoes, insects, and other harmful bio species.[28] Therefore, to stop WH's growth, researchers are now planning to explore the possibilities for economic utilization of WH biomass in various ways, and thus, any fruitful use of this aquatic plant will really

be considered as "waste to wealth" conversion. In that direction, the present study utilizes WH fibers to synthesize the engineered microstructure of LLZO cubic garnet for its use in all solid-state batteries.

METHODOLOGY

WH plants were collected from local water bodies, and the green petioles were cut into pieces. The petioles were first cleaned thoroughly with deionized water followed by dilute acid and alkali solution to remove impurities. The cleaned petioles were then oven-dried at 250 °C for about 3−4 h and ground to powder. The WH powder was kept in a desiccator to avoid moisture contamination. Stoichiometric amounts of $LiNO_3$, $La(NO_3)_3$, $ZrO(NO_3)_2$, and $Ga(NO_3)_3$ were taken, considering a nominal composition of $Li_{6.25}La_3Ga_{0.25}Zr_2O_{12}$ (with 10% excess Li) along with alanine as a complexing agent in an aqueous medium. The mixture was heated with constant stirring on a hot plate at 150−250 °C to obtain a clear viscous gel (henceforth referred as Ga-LLZO-Gel). The Ga-LLZO-Gel was then mixed with the WH fiber in a 10:1 v/w ratio and ball-milled for 12−24 h. The milled slurry was pre-calcined at 500 °C and finally at 900 °C for 5 h in air to obtain cubic WH-Ga-LLZO powder. The different steps involved in the synthesis process are schematically presented in Figure 1.

The thermogravimetric measurements were carried out using a thermal analyzer (NETZSCH, Germany) under air atmosphere with a constant heating rate of 10 °C/min from RT-1200 °C for pristine fiber, Ga-LLZO-Gel, and gel-loaded WH fiber. X-ray diffractograms were collected using an X'pert Pro MPD XRD system (PANalytical, Netherlands) with nickel-filtered Cu Kα (λ = 1.5406 Å) radiation and irradiated at 40 kV and 40 mA with a step size of 0.02 to investigate the purity of phases present in the WH fiber and powder. The quantitative phase estimation was carried out using XRD data of calcined and sintered Ga-LLZO samples using PANalytical X'pert Highscore Plus software. To identify phases in calcined powders, the Raman spectroscopy was carried out using a Horiba LaBRam HR Evolution Raman spectrometer under a

488 nm Ar ion laser of 20 mW power. The FTIR spectrum was carried out using a JASCO FTIR-6300 spectrometer. The microstructure and morphology of the WH fiber and WH-Ga-LLZO samples were analyzed using a scanning electron microscope (SEM, Phenom TM, Model Pro-X, USA) and field emission scanning electron microscope (FESEM, Supra VP35 Carl Zeiss, Germany) respectively. Transmission electron microscopy (TEM) was also carried out for the bulk powders (WH-Ga-LLZO) calcined at 900 and 1000 °C using a Tecnai G2 30ST (FEI) microscope operated at an accelerating voltage of 300 kV to further understand the microstructural features along with the elemental composition.

The Li ion conductivity of WH-Ga-LLZO pellets sintered at 900, 1000, 1100, and 1200 °C in air were measured by AC electrochemical impedance spectroscopy (EIS) with an Autolab potentiostat over a frequency range of 0.1 Hz to 1 MHz by applying a 10 mV AC amplitude at room temperature. Before the measurement, parallel surfaces of sintered pellets were coated with Ag paste. The spectra obtained for the pellets were analyzed using ZView software by fitting the depressed semicircles.

Once the conductivity measurement was completed, the pellets sintered at 1000 °C were fractured for examining the microstructure in FESEM, and corresponding EDX was also carried out for elemental analysis. XRD was performed to identify the phases present in sintered pellets.

To evaluate the galvanostatic cycling performance, lithium symmetric cells with a configuration of Li/WH-Ga-LLZO/Li was fabricated inside a glove box, attaching two lithium metal foils on both surfaces of the WH-Ga-LLZO pellet sintered at 1000 °C. The dimension of the pellet, as measured, was 0.6 mm in thickness and 7.98 mm in diameter. Before making the symmetric cell, both sides of the pellet were polished to remove surface impurities and soaked with IL (LiTFSI: lithium bis(trifluromethylsulfonyl)imide, 99%, Iolitec Ionic Liquid Technologies GMBH, Tetraglym: tetraethylene glycol dimethyl ether, 99%, Acros Organic, mixing ratio of 1:1 w/v %) for good wettability of the lithium metal foil. The sandwich-type cell was crimped in a 2032 coin cell configuration for testing in an automated battery tester Arbin, USA. The cells were galvanostatically charged/discharged at step current densities of 28−452 $\mu A/cm^2$ at an interval of 50 cycles in each current densities using the following program: [charging at +28 $\mu A/cm^2$, 30 min], rest (10 min), [discharging at −28 $\mu A/cm^2$, 30 min], rest (10 min), voltage range of ±1.0 V. The cycled symmetric cell was further dismantled for examining lithium dendritic penetration under FESEM.

RESULTS AND DISCUSSION

Thermal Analysis. The major components in raw WH biomass are 20% cellulose, 33% hemicellulose, and 10% lignin as estimated by Bolenz et al.,[29] Poddar et al.,[30] and Gressel et al.[31] Therefore, the study of thermal behavior of raw WH fiber is necessary before conducting the exo-templating process. It is also required to estimate the ash content in WH fiber after thermal treatment. The thermal analysis was carried out using TGA-DTA for raw WH fibers (oven-dried at 250 °C for 4 h) from RT to 1200 °C at a heating rate of 10 °C/min in air as presented in Figure 2a. The profile revealed three distinct weight losses of 10%, 85%, and 91% at temperatures of around 250, 535, and 900 °C, respectively. From RT to 250 °C, the initial weight loss of 10% corresponds to the removal of water from WH fibers. Thereafter, the decomposition of cellulose,
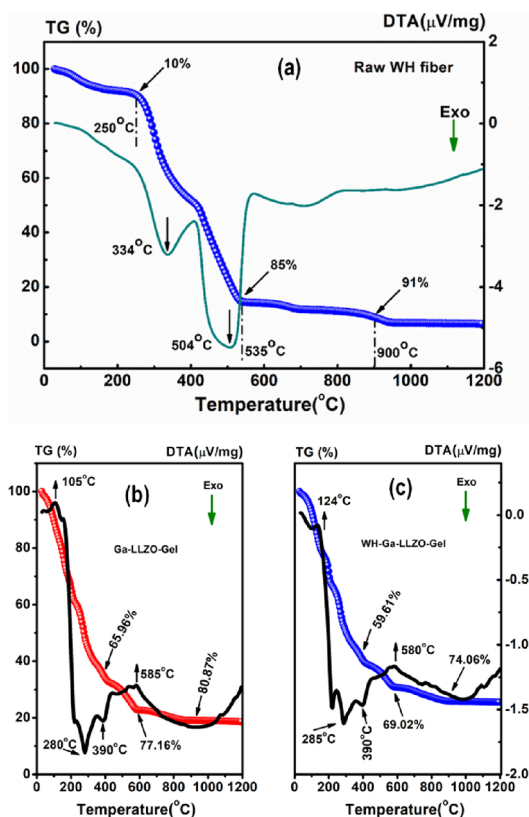
Figure 2. TGA and its corresponding DTA plots of (a) raw WH fiber, (b) Ga-LLZO-Gel, and (c) WH-Ga-LLZO-Gel from RT to 1200 °C.

hemicellulose, and lignin in WH fibers takes place, which was reflected by two exothermic peaks at 334 and 535 °C in the DTA curve. The weight loss continued up to 900 °C resulting in a total weight loss of 91%. No significant weight loss could be observed at up to 1200 °C. From the above thermogram, the ash content in raw WH fiber was estimated to be around 9% at up to 900 °C. It also suggested that the alkali and acid pre-treatment might be able to remove some impurities.[32−34] However, the intrinsic metallic elements present in WH fiber that converted into metal oxide during thermal treatment remained as residual ash. The elemental composition of the ash is presented in Figure S1.

Figure 2b,c describes the thermal behavior of Ga-LLZO-Gel produced by dehydrating the stoichiometric mixture of nitrate salts of Li, La, Zr, and Ga in an aqueous medium using alanine as a chelating agent and WH fiber-mixed Ga-LLZO-Gel (10:1 v/w %), termed as WH-Ga-LLZO-Gel. The thermal decomposition profile of Ga-LLZO-Gel showed multi-step weight losses at up to 900 °C. An initial sharp weight loss measuring ∼66% at up to 400 °C was attributed to the exothermic decomposition of nitrates and metal−alanine complexes followed by another weight loss of 11% at up to 585 °C that was due to the formation of the tetragonal phase of Ga-doped LLZO accompanied by the release of absorbed CO_2 and atomic rearrangement of the pyrochlore $La_2Zr_2O_7$ phase.[35] A weight loss estimated to be ∼4% in the temperature range of 585−900 °C was assigned to the phase transition from a tetragonal to a cubic phase in Ga-doped LLZO, which was also reflected by the corresponding endothermic peak at ∼585 °C in the DTA curve. No significant weight loss could be detected after 900 °C for Ga-LLZO-Gel as shown in Figure 2b. The thermal profile of WH fiber mixed with Ga-LLZO-Gel
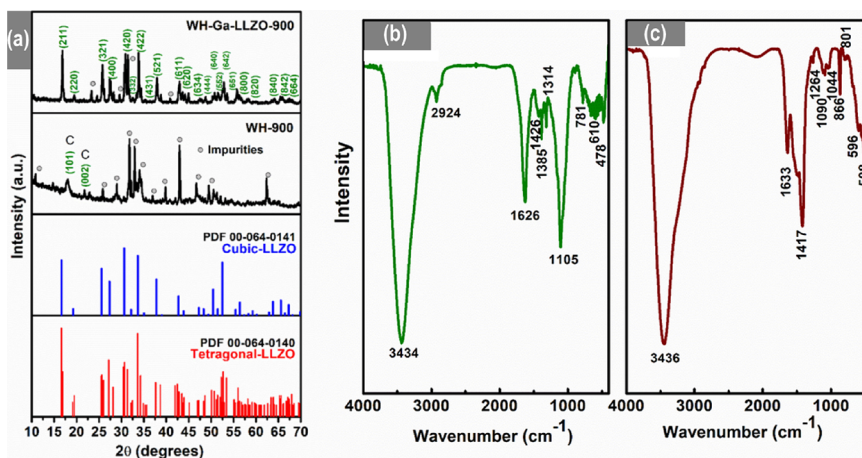
Figure 3. (a) X-ray diffractograms of raw WH fiber and WH-Ga-LLZO powders calcined at 900 °C for 5 h in air. Standard JCPDS data files corresponding to cubic and tetragonal polymorphs of LLZO are also included as reference and cubic phase peaks are indexed in WH-Ga-LLZO calcined powder. The gray solid dots represent the probable impurities such as PbO_2, MgO, CdO, Fe_3O_4, Mn_3O_4, Cr_2O_3, etc., found in calcined WH fiber. (b) FTIR spectra of raw WH fiber and (c) FTIR spectra of WH-Ga-LLZO powder calcined at 900 °C.

(WH-Ga-LLZO-Gel) also followed a similar trend to that of Ga-LLZO-Gel as shown in Figure 2c. No significant change in the nature of the thermal profile could be observed apart from a slight difference in the total weight loss of ∼6% compared to Ga-LLZO-Gel, which might have arisen from the presence of impurities in raw WH fiber (ash content).

Structural Analysis. X-ray diffractograms of WH fiber and WH-Ga-LLZO both calcined at 900 °C for 5 h in air are presented in Figure 3a along with standard JCPDS files of cubic-LLZO (PDF no. 00-064-0141) and tetragonal-LLZO (PDF no. 00-064-0140). The WH fibers showed two small peaks at 2θ = 17.9° and 21.7°, which correspond to the 101 and 002 planes of crystalline cellulosic phases.[36] Several other peaks were found in the calcined powder of WH fibers, which might have originated from inherent metal oxide impurities such as PbO_2, MgO, CdO, Fe_3O_4, Mn_3O_4, Cr_2O_3, etc.[14] The quantitative phase analysis of the powder XRD pattern of WH-Ga-LLZO powder calcined at 900 °C revealed the presence of both cubic (42.5%) and tetragonal (56.9%) LLZO phases along with trace amounts of non-detectable impurities.

To further confirm the phases, Raman spectra was recorded for WH-Ga-LLZO-900 calcined powder. It is reported that the LLZO tetragonal phase shows a higher number of spectral features compared to its cubic polymorph due to its distorted Li^+ ion arrangement and/or lower symmetry.[37] The Raman spectra as observed in Figure S4a could be typically categorized in three regions: (i) a low-frequency region below 300 cm^{-1} responsible for translational modes of mobile cations, (ii) an intermediate-frequency range between 300 and 550 cm^{-1} where the cubic phase exhibits a broad and partly overlapping band and the tetragonal phase shows a higher number of peaks, and (iii) the high-frequency range above 550 cm^{-1} that could be assigned to the vibrational stretching of ZrO_6 octahedra. In Figure S4a, at a low-frequency region, a number of peaks were found at 96, 159, 178, 191−, and 258 cm^{-1}, representing the existence of a tetragonal phase along with a cubic phase, which showed broad and overlapping peaks characteristic of cubic-phase LLZO in the intermediate region. Apart from these two phases, the possible appearance of impurity phases particularly Li_2CO_3 during the calcination process of the LLZO garnet material is unavoidable, and they are treated as surface contaminants for LLZO.[38−41] It is also believed that Li_2CO_3

formation occurred between interactions of H_2O and LLZO through a Li^+/H^+ exchange when exposed to an ambient atmosphere.[39−41] Although trace surface contamination of Li_2CO_3 could not be verified by XRD, it was detected during FTIR analysis as presented in the next section. A very minute quantity of constituent oxide such as La_2O_3 could also be present in the calcined powder, which formed due to loss of lithium at high temperature. It was previously observed in TGA analysis that WH fiber produces an ash amounting to ∼9 wt % in the final product powder when calcined at 900 °C (see Figure 2a). Thus, the appearance of few unknown metal oxide peaks in the diffractogram of WH-Ga-LLZO-900 possibly originated from the ash of WH fiber.

FTIR spectroscopy was carried out to identify the changes in (a) raw WH fiber dried at 250 °C and (b) WH-Ga-LLZO powder after being calcined at 900 °C. WH fiber consists of three main functional groups, namely, cellulose, hemicelluloses, and lignin along with metal salt impurities. The characteristic peaks of cellulose, lignin, and hemicelluloses for WH-fiber were thus reflected in the spectra as shown in Figure 3b at peak positions 1626, 1426, 1314, 1105 cm^{-1}.[36,42] A broad peak appeared at 3434 cm^{-1} and was assigned to the O−H vibration of absorbed water by the fiber.[43,44] Several minor peaks were also recorded at 781, 610, and 478 cm^{-1}, which might have originated from the metal oxide impurities in the fiber. The FTIR spectra of exo-templated WH-Ga-LLZO powder calcined at 900 °C is shown in Figure 3c. Similar to that of WH fiber, distinct peaks of O−H vibration were also observed at 3436 and 1633 cm^{-1} due to absorbed moisture by WH-Ga-LLZO calcined powder. The LLZO powder readily reacts with moisture and spontaneously takes part in Li^+/H^+ ion exchange to form a surface-active Li_2CO_3 layer.[40] In Figure 3c, two distinct characteristics peaks of Li_2CO_3 were also detected at peak positions 1417 and 866 cm^{-1}, suggesting the formation of the surface-active Li_2CO_3 phase in WH-Ga-LLZO.[45] Such surface contamination is unavoidable and s responsible for lowering ionic conductivity in the garnet. The spectra also reflected two minor peaks that appeared at the lower-wavenumber region of 596 and 508 cm^{-1} and assigned to M−O vibrations of Zr−O and La−O, respectively.[46] The FTIR findings obtained in the present study are summarized in

Table 1. Peak Positions and Their Corresponding Assignment for Raw WH Fiber and WH-Ga-LLZO Powder Calcined at 900 °C

| raw WH fiber		WH-Ga-LLZO	
peak position (cm^{-1})	peak assignment	peak position (cm^{-1})	peak assignment
3434 (broad, sharp)	O−H stretching, moisture	3436 (broad, sharp)	O−H stretching, moisture
2924 (narrow, sharp)	C−H stretching, cellulose	1633 (sharp)	δ (H$_2$O) absorbed moisture
1626 (sharp)	C=O vibration, characteristic group of lignin and hemicellulose	1417 (sharp)	C−O stretching, characteristic peak of Li$_2$CO$_3$
1426 (minor)	C−H bending, the presence of lignin contents in the fiber or C−O cellulose	1264 (minor)	unknown
1385 (minor)	O−H organic/phenolic type	1090 (minor)	unknown
1314 (minor)	characteristic group of lignin and hemicellulose, C−H	1044 (minor)	unknown
1105 (sharp)	−C−O−C vibration in cellulose and hemicelluloses	866 (sharp)	C−O stretching, characteristic peak of Li$_2$CO$_3$
781 (minor)	unknown	801 (minor)	unknown
610 (minor)	unknown	596 (minor)	Zr−O characteristic band
478 (minor)	unknown	508 (minor)	La−O vibration
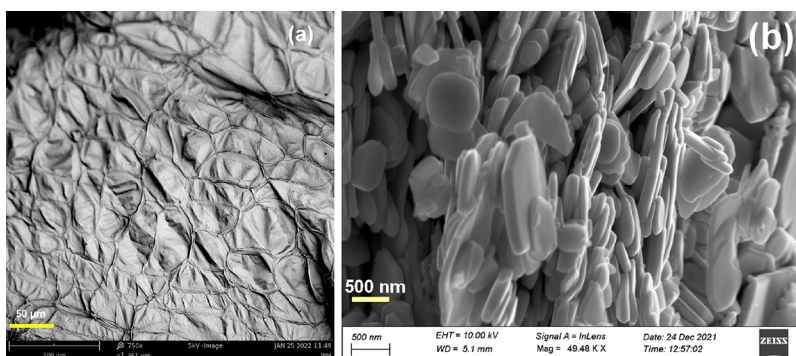
Figure 4. (a) SEM micrograph of WH dried petioles and (b) FESEM image of WH-Ga-LLZO powder calcined at 900 °C.
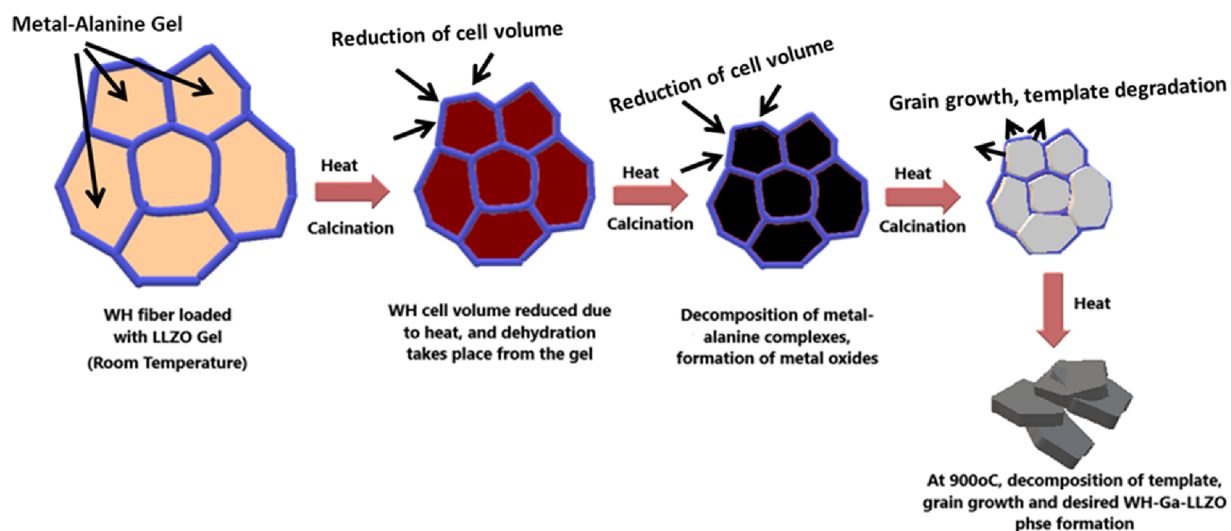
Figure 5. Schematic illustration of the origin of the plate-like morphology of WH-Ga-LLZO powder calcined at 900 °C. The color of the impregnated gel gradually changes to a darker shade as the temperature increases prior to decomposition and nucleation.

Table 1, describing peak positions and their corresponding peak assignment.

Origin of Microstructure. In exo-templating synthesis methodology, the process and place (i.e., confined space) of impregnation of the precursor gel inside the targeted template play an important role for defining the particle's morphology.

Inside the WH petiole fibrous unit, two confined spaces are available for gel impregnation, namely, vascular tissue xylem and aerenchyma cells. In our previous studies on BBCF-based MIEC membranes, we carefully impregnated BBCF precursor gel into the empty tubular spaces confined by the cell walls of WH fiber.[14] Controlled heat treatment for removal of template

thus resulted in nanorod-like BBCF morphology. In the present study, we attempted to load the gel in aerenchyma cells (a tissue with large, empty, and polygonal cell structure) to mimic its polygonal pattern. Polygonal shaped aerenchyma cells with discrete cell boundaries was observed in the SEM image as given in Figure 4a, which resulted in multifaceted "plate-like" morphology after exo-templating. Figure 4b shows the FESEM micrograph of WH-Ga-LLZO calcined powder showing plate-like particles with an average thickness of 100−120 nm. Such a unique morphology in WH-Ga-LLZO powder might have originated from mimicking the polygonal shaped arrenchyma cells present in the WH fiber, which provided a scaffold for synthesis of Ga-LLZO. The formation mechanism of plate like morphology has been illustrated schematically in Figure 5. As shown in Figure 5, at room temperature, during the gel loading process, the cellular confined space of WH fiber becomes filled with the constituent's gel of LLZO. On heat treatment, two processes simultaneously occur: (1) thermal shrinkage of the WH template and (2) dehydration of aqueous LLZO-Gel in the confined space. Therefore, a reduction in WH template dimension (volume) is expected, whereas the volume of the gel is also reduced due to the removal of water from its matrix. On further heating, the gel decomposition starts resulting in nucleation and grain growth of the desired phase inside the thermally squeezed template. On further increasing the calcination temperature, the WH scaffold or template is finally removed, producing a plate-like exo-templated microstructure of LLZO garnet. As shown in the SEM micrograph of Figure 4a, the raw WH fiber showed an average length of the template of around 50−100 μm; however, the 900 °C calcined LLZO powder revealed a plate-like morphology with an average length scale of 0.5−1.0 μm (Figure 4b). The reason behind of such a reduction in the length scale from raw fiber to calcined powder was the dimensional shrinkage of the template at high temperature as explained above. It is worth mentioning here that the use of WH fiber as an exo-template can offer typically two types of morphologies: (a) when the gel impregnation occurs in the tubular xylem of WH fiber, it produces nanorods,[14] and (b) when the gel loading is done inside aerenchyma cells, it develops a "plate-like" morphology as observed in WH-Ga-LLZO calcined powder. This formation process of nanorods and plate-like morphology is illustrated schematically in Figure 6 for understanding of the above phenomena happening during the gel loading process.

For further analysis of the microstructure and morphology, TEM images were taken for WH-Ga-LLZO powders calcined at 900 and 1000 °C along with their elemental compositions using EDX, and the micrographs are presented in Figure S5a−d. The average particle size as measured for 900 °C-calcined powder was found to be less than 100 nm. The presence of an agglomerated morphology could also be visible in Figure S5a. The elemental composition as shown in Figure S5b revealed the presence of La, Zr, and Ga along with trace amounts of Al that likely originated from the Al crucible during calcination. In Figure S5c, a discrete plate-like morphology of WH-Ga-LLZO powder calcined at 1000 °C could be identified. The thickness of oriented plates was measured in the range of 40−120 nm. The EDX profile as shown in Figure S5d was found to be similar in nature to that of WH-Ga-LLZO powder calcined at 900 °C. The cryptographic information by analyzing HRTEM could not be realized this time due to electron beam irradiation
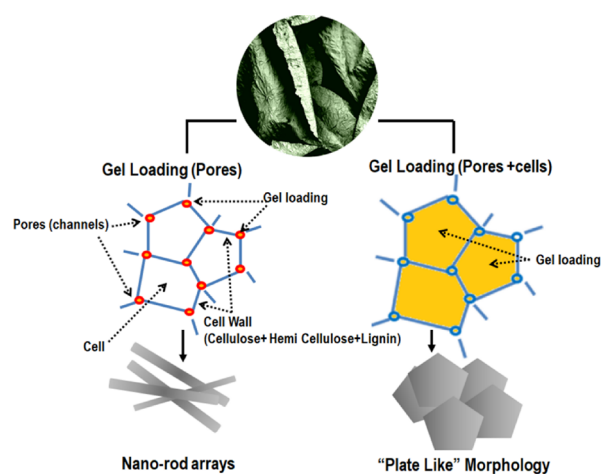

Figure 6. Schematic representation showing the proposed path to obtain (left) nanorod arrays[14] and (right) "plate-like" morphology via the exo-templating method mimicking intercellular structures (pore channels for nanorod arrays and aerenchyma cells for the plate-like morphology) of WH fiber.

damage to the samples. It needs further refinement in imaging parameters and the specimen preparation procedure.

Electrochemical Performance. Figure 7 shows the room-temperature AC impedance plots of WH-Ga-LLZO pellets sintered at (a) 900 °C, (b) 1000 °C, (c) 1100 °C, and (d) 1200 °C in air. All the profiles comprise of two depressed semicircles along with a diffusion tail: the first semicircle that appeared at a low-frequency region is due to the contribution of the grain boundary, and the second at a high frequency is attributed to the grain or bulk properties of WH-Ga-LLZO pellets. The appearance of a straight-line tail at a lower frequency using Li-ion blocking Ag electrodes suggests that the synthesized WH-Ga-LLZO garnet is intrinsically Li ion-conductive in nature.[47] An equivalent circuit model comprising circuit elements $R_e(R_b CPE_b)(R_{gb} CPE_{gb})$ has been used here to fit the curves as shown in the inset of Figure 7a−d where R_b, R_{gb}, and R_e are the resistances representing bulk, grain boundaries, and Ag electrodes; CPE_b and CPE_{gb} represent constant-phase elements that originated from grain and grain boundaries. The total conductivity is determined by adding R_b and R_{gb}. The contribution of grain and grain boundaries in total conductivity of WH-Ga-LLZO pellets sintered at different temperatures is summarized in Table S1. The conductivity values (S/cm) were calculated using the equation, $\sigma = \frac{1}{R} \cdot \frac{l}{A}$ where R is the resistance, l is the thickness, and A is the area of the pellets. The sintering temperature versus conductivity values, which include σ_b, σ_{gb}, and σ_{total}, are plotted in Figure 8. The plot showed that the highest bulk conductivity (σ_b) value of 3.94×10^{-5} S/cm could be obtained for the WH-Ga-LLZO sample sintered at 1000 °C. We also observed that the bulk conductivity (σ_b) gradually reduces as the sintering temperature increases. On the other hand, with the increase in sintering temperature from 900 to 1000 °C, the grain boundary resistance initially decreased; however, no further significant reduction in impedance could be observed on elevated sintering temperatures. This may be due to the fact that, with an increase in sintering temperature, a slight stoichiometric loss of lithium may result in the appearance of secondary phases, which may accumulate at the grain boundary blocking lithium ion migration. To identify the phases, present
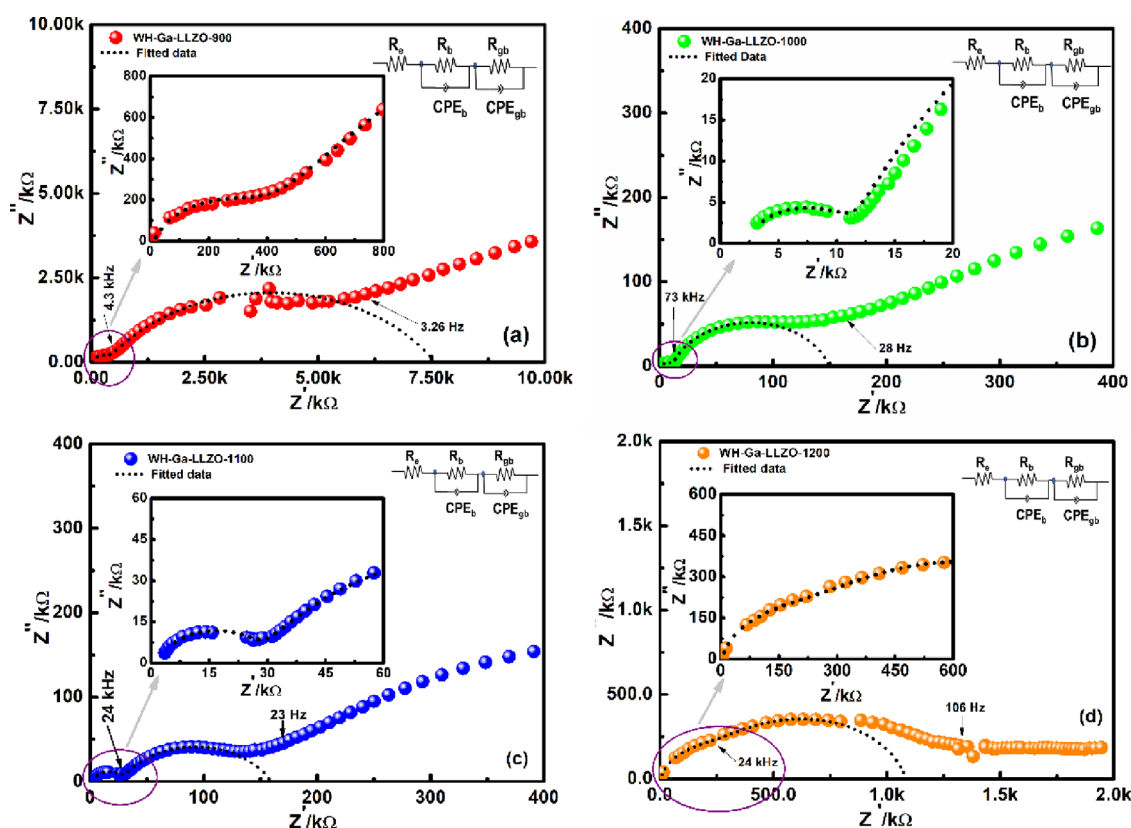
Figure 7. Room temperature AC impedance plots of WH-Ga-LLZO pellets sintered at (a) 900 °C, (b) 1000 °C, (c) 1100 °C, and (d) 1200 °C. The inset shows the corresponding equivalent circuit.
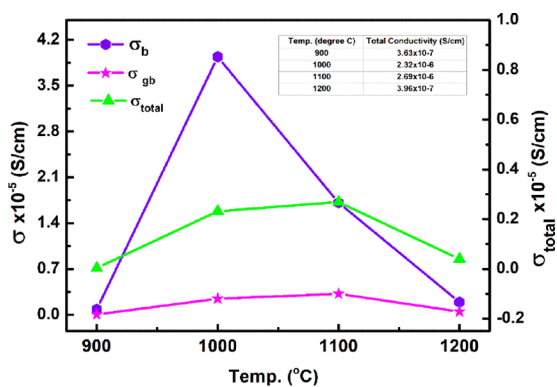

Figure 8. Plot showing variation of grain, grain boundary, and total conductivities of the pellets w.r.t sintering temperatures (900, 100, 1100, and 1200 °C).

the major phase is cubic amounting to 71.6% with a 25.8% Li_2CO_3 surface impurity phase, which appeared during the post-sintering stage due to an unavoidable surface reaction.[40] The cubic phase of sintered at 1000 °C was further confirmed by Raman spectroscopy as shown in Figure S4b, which indicated a lesser number of peaks characteristic to the cubic LLZO-type phase.[37] With an increase in the sintering temperature at 1100 °C, the amount of cubic phase reduced to 63.3% along with Li_2CO_3 (32.3%) and trace amounts of other oxide impurities. At 1200 °C, the cubic phase was found to have transformed into a pyrochlore-type $La_2Zr_2O_7$ phase (24.2%), $La(OH)_3$ (34.5%), and Li_2CO_3 (31.8%) phase.

In summary, EIS results revealed that the maximum exhibited total Li-ion conductivity (bulk + grain boundary) was found to be 2.69×10^{-6} S/cm for Ga-LLZO pellets sintered at 1100 °C, whereas the highest bulk conductivity of 3.94×10^{-5} S/cm could be measured in the pellets sintered at 1000 °C. A similar kind of trend in bulk conductivities was also observed by Afyon et al. due to a slight reduction of density from 76% at 950 °C to 69% at 1100 °C for the Ga-doped LLZO sample synthesized by a modified sol–gel method.[48] The total conductivity value appeared to be somewhat lower than the previously reported literature values for Ga-doped LLZO with similar compositions, which might be due to the poor densification of the WH-Ga-LLZO pellets.[49−52] The presence of a large number of voids was confirmed by FESEM micrographs on a fractured surface of the pellets sintered at 1000 °C as shown in Figure 9b with a corresponding EDX profile. Elemental mapping carried out on the fractured surface of the pellet is also given in Figure 9c, describing the presence
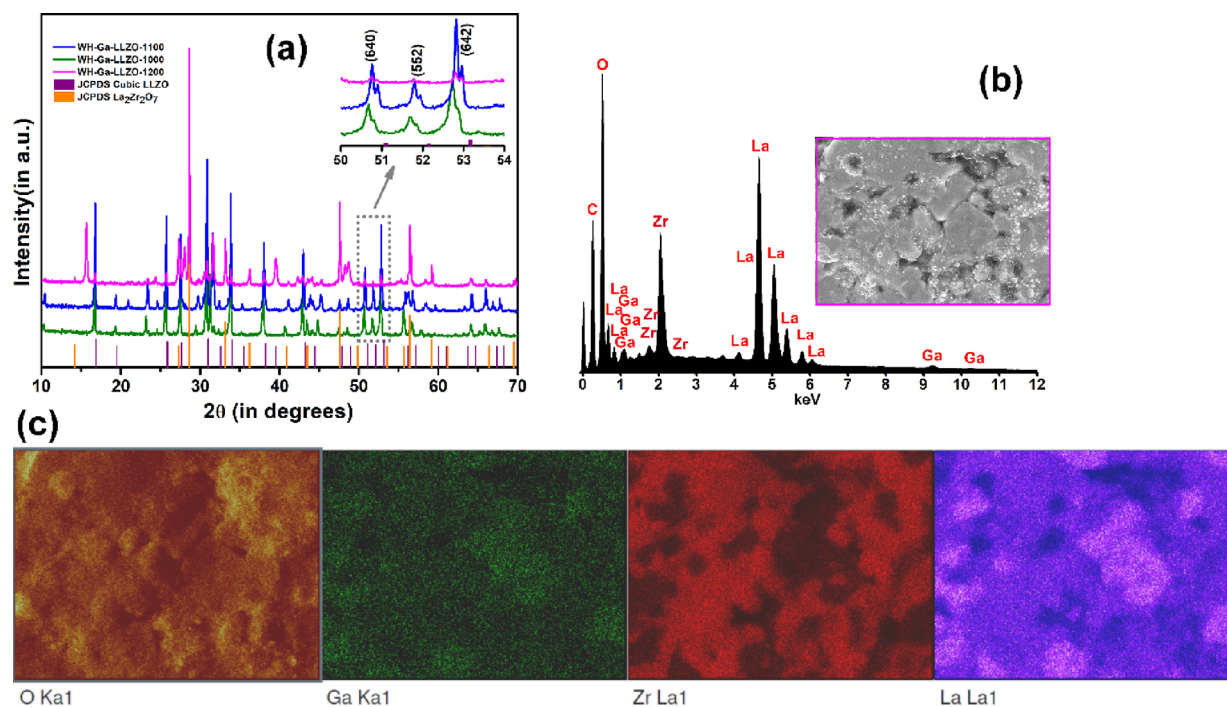
in the pallets sintered at 1000, 1100, and 1200 °C, XRD was performed and the corresponding X-diffractograms are shown in Figure 9a. The XRD profile of the pellet sintered at 1000 °C showed all the major peaks assigned for cubic garnet; however, with an increase in sintering temperature, pyrochlore-type $La_2Zr_2O_7$ phases started appearing visibly in the inset of Figure 9a. It was observed that the magnitude of splitting of peaks (640, 552, and 642 peaks) in the cubic phase of LLZO gradually increases with the increase in sintering temperature. A phase transformation from a cubic to a pyrochlore-type structure could be observed for the pellet sintered at 1200 °C. To further confirm the phases formed at different sintering temperatures of 1000, 1100, and 1200 °C, quantitative phase analysis was carried out. The results revealed that, at 1000 °C,

Figure 9. (a) XRD diffractograms of WH-Ga-LLZO pellets sintered at 1000,1100, and 1200 °C in air, (b, c) EDX profile and elemental map of O, La, Ga, and Zr taken at the fractured surface of the WH Ga-LLZO pellet sintered at 1000 °C in air.

of constituent elements both at grain and grain boundaries in the fractured surface apart from void areas.

Symmetric Cell and Current Density. To evaluate the galvanostatic cycling performance with a configuration of Li/ WH-Ga-LLZO/Li, a lithium symmetric cell was fabricated and tested by step ascending current densities at room temperature. For that purpose, in the present study, we have introduced ionic liquid (IL) to effectively reduce the interfacial resistance and enhance the interfacial stability of metallic Li at both surfaces of WH-Ga-LLZO pellets. Ionic liquids (ILs) offer intrinsic ionic conductivity and its use is considered as one of the best well-known procedures where one can achieve good interfacial wettability of a lithium metal anode with an LLZO SSE garnet.[53,54] The galvanostatic cycling performance of lithium symmetric cells tested at different current densities are presented in Figure 10a. The initial current density was fixed to 28 μA/cm^2 and gradually increased every after completion of 50 cycles. The cycles were performed with an initial set program of [charging at +28 μA/cm^2, 30 min], rest (10 min), [discharging at −28 μA/cm^2, 30 min], rest (10 min), voltage range ±1.0 V. The positive and negative potentials in the curve signify the corresponding Li stripping and plating processes. It was observed that, at a lower current density of 28 μA/cm^2, the cell performed a lithium stripping/plating process continuously up to 50 cycles with stable polarization. With further increase in the current density step-wise, smooth cycling profiles were recorded. The enlarged view of cycling profiles at ascending current densities as marked I to V in Figure 10a by dotted lines are presented in Figure 10b, describing the symmetrical polarization during the lithium stripping/plating process. At a high current density of 452 μA/ cm^2, a large polarization could be detected, which might have originated from the loss of contact of the Li electrode to the solid electrolyte surface, which increased the lithium/electrolyte interfacial resistance. This is a very common issue faced

during cycling of garnet electrolytes because of the poor contact wettability and lack of interphase between the Li metal and electrolyte.[55−57] A drastic increase in polarization, instead of a short circuit, forced the cell to be disconnected after completion of 295 h of the lithium stripping/plating process. To measure the effect of dendritic penetration of the metallic lithium anode to the WH-Ga-LLZO solid-state electrolyte, impedance spectroscopy was taken for the symmetric cell before and after lithium plating, and the spectra is given in Figure 10c. It described that the total conductivity of the WH-Ga-LLZO electrolyte slightly increases from 1.04 ×10^{-4} S/cm to a value of 1.6 × 10^{-4} S/cm after 250 cycles (295 h). This may be due to the fact that the penetration of the lithium metal through the grain boundary of the WH-Ga-LLZO electrolyte might be sluggish in nature. It is also proposed that the unique plate-like grain might be responsible for the increase of the lithium dendritic diffusion path length through grain boundaries. However, to understand the lithium deposition through grain boundaries in WH-Ga-LLZO, the cycled cell was dismantled, and the pellets were examined under FESEM as shown in Figure 11a−d, respectively. A significant change in color of both the surfaces of the cycled pellets was observed. The black spots were found at places on the surfaces suggesting the point of metallic contacts or growth. The FESEM micrographs of top and fracture surfaces as shown in Figure 11c,d, revealed that the primary grain structure as seen before plating was found to be somewhat distorted from its original structure (as shown in Figure S2). This may be due to the penetration of a metallic anode through grain boundaries or voids during cycling. Very few numbers of microcracks were found in the grain boundary region of cycled pellets as seen in the FESEM micrographs of the fracture surface of the cycled pellet, which might be due to the dendritic penetration of metallic lithium across the grain boundary. The EDX spectrum taken at the fractured surface of cycled WH-Ga-LLZO pellets
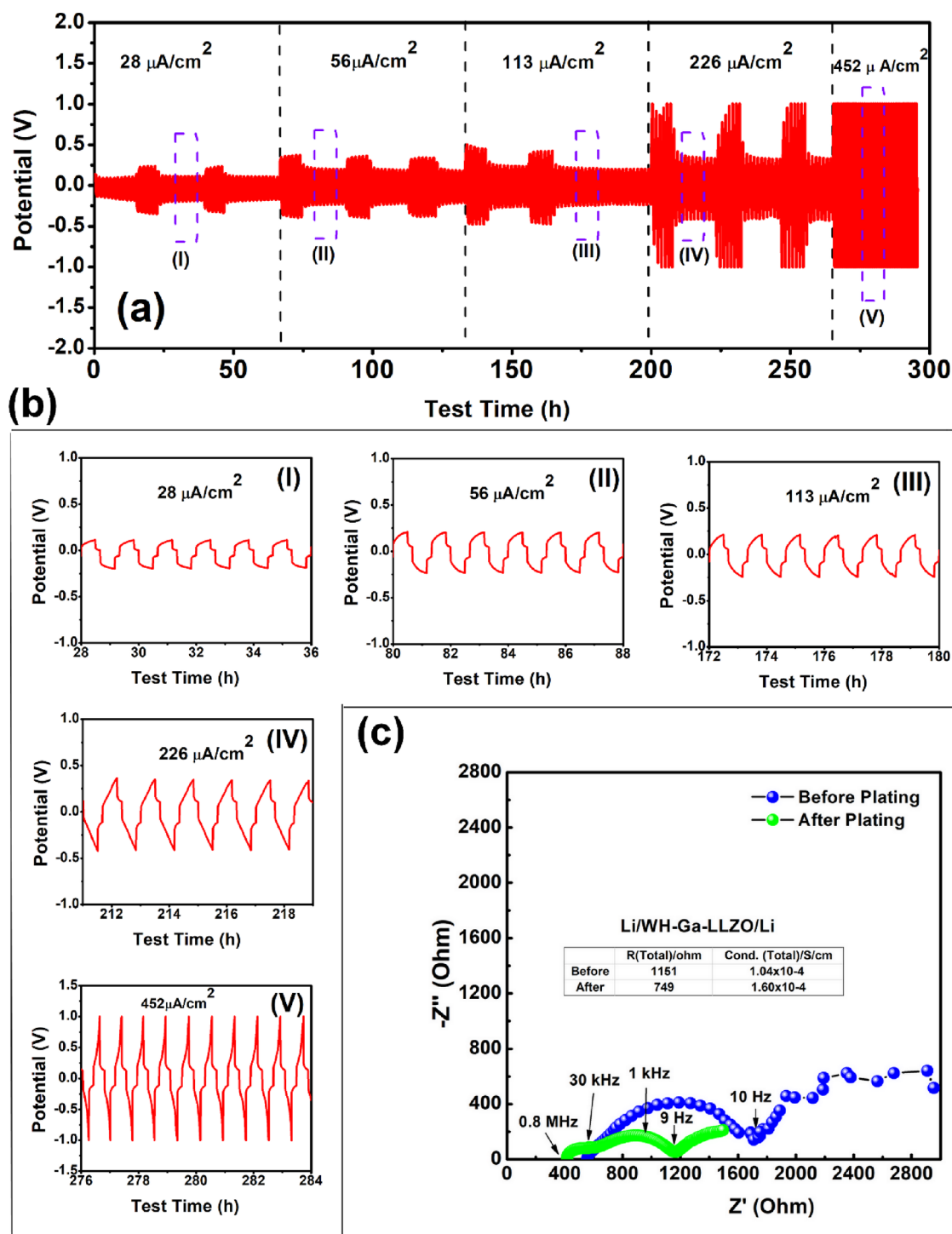
Figure 10. Electrochemical galvanostatic profile of Li/WH-Ga-LLZO/Li symmetric cell (a) at various current densities from 28 to 452 $\mu A/cm^2$. (b) Enlarged cycling profiles marked as (I−V) in a. (c) Electrochemical impedance plot of a symmetric cell before and after plating.

also presented Figure S3 to better understand the topographic change in grains and grain boundaries. It showed that no significant changes either in the grain structure or elemental homogeneity of the WH-Ga-LLZO electrolyte could be found. The unique microstructure as obtained through the exo-templating process possibly hindered the dendritic migration of metallic anode in the WH-Ga-LLZO electrolyte by increasing the diffusion path length across the grain boundaries. The increased polarization with incremental current densities without a short circuit in the fabricated

lithium symmetric solid-state cell, comprising the WH-Ga-LLZO electrolyte, might be due to the effect of a unique microstructure obtained by the exo-templating process, as presented and illustrated schematically in Figure 11e.

■ CONCLUSIONS

The present research successfully used a biowaste material for making a cubic Ga-doped LLZO ($Li_{6.25}La_3Ga_{0.25}Zr_2O_{12}$) solid-state electrolyte for application in all solid-state lithium batteries (ALSSBs). The developed exo-templating method
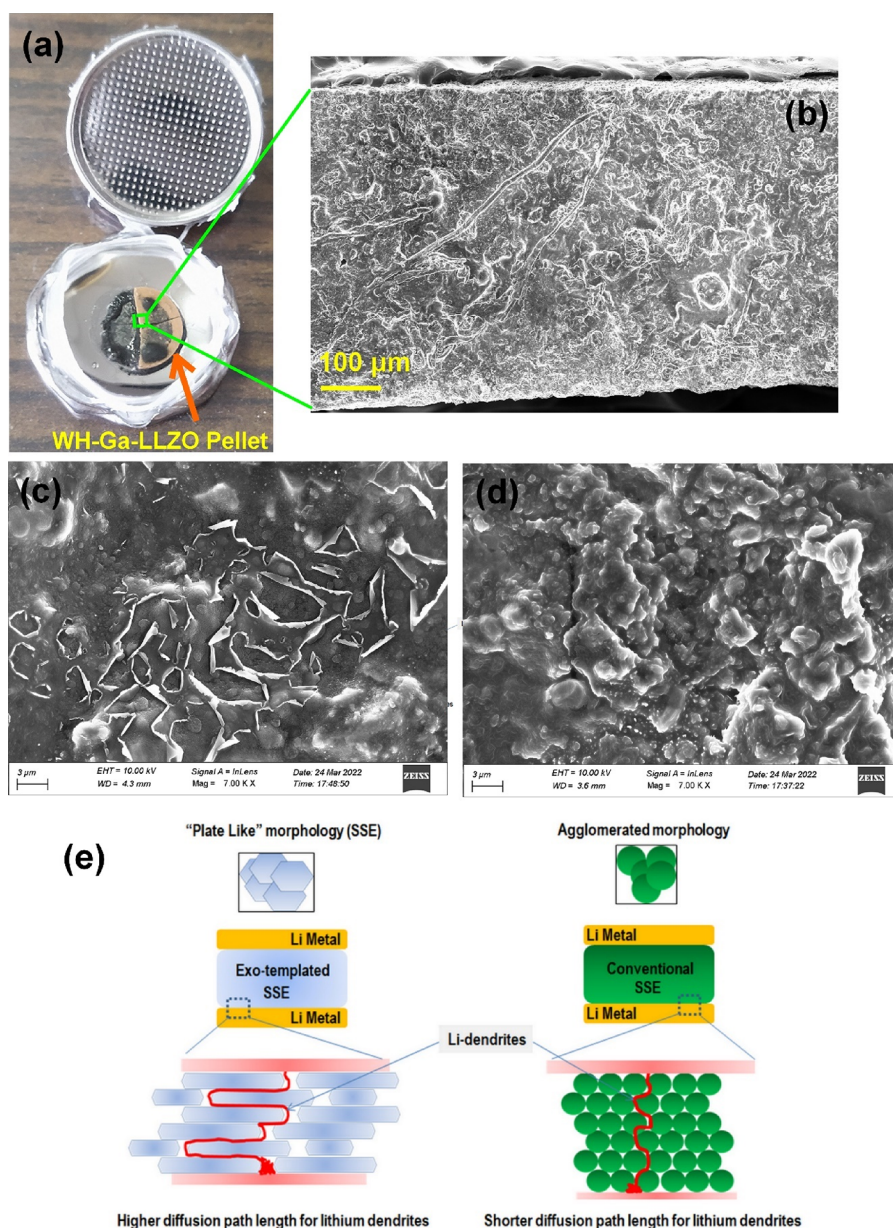
Figure 11. (a) Dismantling of 2032 coin cells after galvanostatic cycling. (b) FESEM micrograph of cycled WH-Ga-LLZO pellets. (c. d) FESEM micrographs of top and fracture surfaces of cycled WH-Ga-LLZO pellets. (e) Schematic illustration of metallic anodic deposition through exo-templated and conventionally a prepared solid-state electrolyte.

resulted in a cubic-phase LLZO at a lower temperature of 1000 °C, which is a far lower temperature than of the conventional solid-state process (>1200 °C) in synthesizing LLZO-based materials. The FESEM micrographs revealed a unique "plate-like" microstructure that originated from mimicking the intercellular polygonal structure of WH fibrous tissues. The synthesized Ga-doped LLZO solid electrolyte showed a bulk Li-ion conductivity in the order of 10^{-5} S/cm. The electrochemical results revealed that the engineered micro-structure played a crucial role during galvanostatic cycling of the cell. The cell assembled with the developed electrolyte cycled 295 h in continues mode with increasing current densities. At a high current density of 452 μA/cm^2, the cell showed symmetric polarization without any short circuits. This intrinsically simple method thus developed using WH as an exo-template can be extended to synthesize other multifunc-tional energy materials with interesting microstructures and enhanced physicochemical properties.

■ ASSOCIATED CONTENT

ⓢ Supporting Information

The Supporting Information is available free of charge at https://pubs.acs.org/doi/10.1021/acsomega.2c04012.

> Variation of conductivity of WH-Ga -LLZO pellets sintered at different temperatures,typical EDX spectrum and its corresponding elemental map showing the presence of different Metal (Ba, K, Al, Ca, P, Mg, and Na) in raw WH fiber calcined at 900 °C, FESEM micrographs of top and fracture surfaces of WH-Ga-LLZO pellets sintered at 1000 °C, typical EDX spectrum of the fracture surface of WH-Ga-LLZO after galvano-static cycling, Raman spectra of WH-Ga-LLZO powders

calcined at different temperatures, and TEM images and corresponding elemental composition (PDF)

AUTHOR INFORMATION

Corresponding Author

Mir Wasim Raja − *Energy Materials and Devices Division (former Fuel Cell and Battery Division), CSIR-Central Glass and Ceramic Research Institute, Kolkata 700032, India;* ⓞ orcid.org/0000-0003-3090-7378; Phone: +91,332,322 3393; Email: mwraja@cgcri.res.in

Author

Kuntal Ghosh − *Energy Materials and Devices Division (former Fuel Cell and Battery Division), CSIR-Central Glass and Ceramic Research Institute, Kolkata 700032, India;* ⓞ orcid.org/0000-0003-2869-2320

Complete contact information is available at:
https://pubs.acs.org/10.1021/acsomega.2c04012

Notes

The authors declare no competing financial interest.

REFERENCES

(1) Shivaji, S.; Madhu, S.; Singh, S. Extracellular synthesis of antibacterial silver nanoparticles using psychrophilic bacteria. *Process Biochem.* **2011**, *46*, 1800−1807.

(2) Stephen, J. R.; Macnaughtont, S. J. Developments in terrestrial bacterial remediation of metals. *Curr. Opin. Biotechnol.* **1999**, *10*, 230−233.

(3) Camaratta, R.; Lima, A. C.; Reyes, M. D.; Hernandez-Fenollosa, M. A.; Messana, J. O.; Bergmann, C. P. Microstructural evolution and optical properties of TiO2 synthesized by eggshell membrane templating for DSSCs application. *Mater. Res. Bull.* **2013**, *48*, 1569−1574.

(4) Kale, G.; Arbuj, S.; Kawade, U.; Kadam, S.; Nikam, L.; Kale, B. Paper templated synthesis of nanostructured Cu−ZnO and its enhanced photocatalytic activity under sunlight. *J. Mater. Sci.: Mater. Electron.* **2019**, *30*, 7031−7042.

(5) Huang, J.; Wang, X.; Wang, Z. L. Controlled Replication of Butterfly Wings for Achieving Tunable Photonic Properties. *Nano Lett.* **2006**, *6*, 2325−2331.

(6) Meyabadi, F. T.; Dadashian, F.; Sadeghi, G. M. M.; Asl, H. E. Z. Spherical cellulose nanoparticles preparation from waste cotton using a green method. *Powder Technol.* **2014**, *261*, 232−240.

(7) Song, P.; Zhang, H.; Han, D.; Li, J.; Yang, Z.; Wang, Q. Preparation of biomorphic porous LaFeO3 by sorghum straw biotemplate method and its acetone sensing properties. *Sens. Actuators, B* **2014**, *196*, 140−146.

(8) Sun, R.-Q.; Sun, L.-B.; Chun, Y.; Xu, Q.-H.; Wu, H. Synthesizing nanocrystal-assembled mesoporous magnesium oxide using cotton fibres as exotemplate. *Microporous Mesoporous Mater.* **2008**, *111*, 314−322.

(9) Dahoumane, S. A.; Yéprémian, C.; Djédiat, C.; Couté, A.; Fiévet, F.; Coradin, T.; Brayner, R. A global approach of the mechanism involved in the biosynthesis of gold colloids using micro-algae. *J. Nanopart. Res.* **2014**, *16*, 2607.

(10) Zhang, C.; Wang, J.; Hu, R.; Qiao, Q.; Li, X. Synthesis and gas sensing properties of porous hierarchical SnO2 by grapefruit exocarp biotemplate. *Sens. Actuators, B* **2016**, *222*, 1134−1143.

(11) Ozin, G. A. Nanochemistry: Synthesis in diminishing dimensions. *Adv. Mater.* **1992**, *4*, 612−649.

(12) Chen, P.; Wu, Q.-S.; Ding, Y.-P.; Yuan, P.-S. Synthesis of SrCrO4 nanostructures by onion inner-coat template and their optical properties. *Bull. Mater. Sci.* **2008**, *31*, 603−608.

(13) Wang, C. S.; Chang, T.-Y.; Lin, T.-Y.; Chen, Y.-F. Biologically inspired flexible quasi-single-mode random laser: An integration of Pieris canidia butterfly wing and semiconductors. *Sci. Rep.* **2014**, *4*, 6736.

(14) Raja, M. W.; Islam, Q. A.; Basu, R. N. Oxygen separation membrane derived from aquatic weed: A novel bio-inspired approach to synthesize BaBi$_{0.2}$Co$_{0.35}$Fe$_{0.45}$O$_{3-\delta}$ perovskite from Water Hyacinth (*Eichhornia Crassipes*). *J. Membr. Sci.* **2017**, *522*, 168−174.

(15) Murugan, R.; Thangadurai, V.; Weppner, W. Fast Lithium Ion Conduction in Garnet-Type Li$_7$La$_3$Zr$_2$O$_{12}$. *Angew. Chem., Int. Ed.* **2007**, *46*, 7778−7781.

(16) Paolella, A.; Zhu, W.; Bertoni, G.; Savoie, S.; Feng, Z.; Demers, H.; Gariepy, V.; Girard, G.; Rivard, E.; Delaporte, N.; Guerfi, A.; Lorrmann, H.; George, C.; Zaghib, K. Discovering the Influence of Lithium Loss on Garnet Li$_7$La$_3$Zr$_2$O$_{12}$ Electrolyte Phase Stability. *ACS Appl. Energy Mater.* **2020**, *3*, 3415−3424.

(17) Li, Y.; Han, J. T.; Wang, C. A.; Xie, H.; Goodenough, J. B. Optimizing Li+ conductivity in a garnet framework. *J. Mater. Chem.* **2012**, *22*, 15357−15361.

(18) Liu, C.; Rui, K.; Shen, C.; Badding, M. E.; Zhang, G.; Wen, Z. Reversible ion exchange and structural stability of garnet-type Nb-doped Li$_7$La$_3$Zr$_2$O$_{12}$ in water for applications in lithium batteries. *J. Power Sources* **2015**, *282*, 286−293.

(19) Deviannapoorani, C.; Dhivya, L.; Ramakumar, S.; Murugan, R. Lithium ion transport properties of high conductive tellurium substituted Li$_7$La$_3$Zr$_2$O$_{12}$ cubic lithium garnets. *J. Power Sources* **2013**, *240*, 18−25.

(20) Dhivya, L.; Janani, N.; Palanivel, B.; Murugan, R. Li+ transport properties of W substituted Li$_7$La$_3$Zr$_2$O$_{12}$ cubic lithium garnets. *AIP Adv.* **2013**, *30*, 82115−82121.

(21) Mann, M.; Küpers, M.; Häuschen, G.; Finsterbusch, M.; Fattakhova-Rohlfing, D.; Guillon, O. Evaluation of Scalable Synthesis Methods for Aluminum-Substituted Li$_7$La$_3$Zr$_2$O$_{12}$ Solid Electrolytes. *Materials* **2021**, *14*, 6809−6825.

(22) Rettenwander, D.; Geiger, C. A.; Tribus, M.; Tropper, P.; Amthauer, G. A Synthesis and Crystal Chemical Study of the Fast Ion Conductor Li$_{7-3x}$Ga$_x$La$_3$Zr$_2$O$_{12}$ with x = 0.08 to 0.84. *Inorg. Chem.* **2014**, *53*, 6264−6269.

(23) El Shinawi, H.; Janek, J. Stabilization of cubic lithium-stuffed garnets of the type "Li$_7$La$_3$Zr$_2$O$_{12}$" by addition of gallium. *J. Power Sources* **2013**, *225*, 13−19.

(24) Kokal, I.; Somer, M.; Notten, P. H. L.; Hintzen, H. T. Sol-gel synthesis and lithium ion conductivity of Li$_7$La$_3$Zr$_2$O$_{12}$ with garnet-related type structure. *Solid State Ionics* **2011**, *185*, 42−46.

(25) Jin, Y.; McGinn, P. J. Li$_7$La$_3$Zr$_2$O$_{12}$ electrolyte stability in air and fabrication of a Li/ Li$_7$La$_3$Zr$_2$O$_{12}$/Cu$_{0.1}$V$_2$O$_5$ solid-state battery. *J. Power Sources* **2013**, *239*, 326−331.

(26) Kim, K.-W.; Yang, S.-H.; Kim, M. Y.; Lee, M. S.; Lim, J.; Chang, D. R.; Kim, H.-S. Cubic phase behavior and lithium ion conductivity of Li$_7$La$_3$Zr$_2$O$_{12}$ prepared by co-precipitation synthesis for all-solid batteries. *J. Ind. Eng. Chem.* **2016**, *36*, 279−283.

(27) Badami, P.; Smetaczek, S.; Limbeck, A.; Rettenwander, D.; Chan, C. K.; Kannan, A. N. M. Facile synthesis of Al-stabilized lithium garnets by a solution-combustion technique for all solid-state batteries. *Mater. Adv.* **2021**, *2*, 5181−5188.

(28) Ndimele, P. E.; Kumolu-Johnson, C. A.; Anetekhai, M. A. The invasive aquatic macrophyte, water hyacinth *Eichhornia crassipes* (Mart.) Solm-Laubach: Pontedericeae: problems and prospects. *Res. J. Environ. Sci.* **2011**, *6*, 509−520.

(29) Bolenz, S.; Omran, H.; Gierschner, K. Treatment of water hyacinth tissue to obtain useful products. *Biowastes* **1990**, *33*, 263–274.

(30) Poddar, K.; Mandal, L.; Banerjee, G. C. Studies on water hyacinth (*Eichhornia crassipes*)-Chemical composition of the plant and water from different habitats. *Indian Vet. J.* **1991**, *68*, 833–837.

(31) Gressel, J. Transgenics are imperative for biofuel crops. *Plant Sci.* **2008**, *174*, 246–263.

(32) Biswas, B.; Banik, A. K.; Biswas, A. B. Comparative study of various pre-treatment techniques for saccharifications of water hyacinth (*eichhornia crassipes*) cellulose. *Int. J. Biotechnol. Trends Technol.* **2015**, *5*.

(33) Kalhorinia, S.; Naseeruddin, S.; Yadav, K. S.; Goli, J. K.; Rao, L. V. Optimization of acid and enzymatic saccharification of lignocellulosic substrate water hyacinth *Eichhornia crassipes*. *Indian Streams Res. J.* **2013**, *3* .

(34) Eshtiaghi, M. N.; Yoswathana, N.; Kuldiloke, J.; Ebadi, A. G. Preliminary study for bioconversion of water hyacinth (*Eichhornia crassipes*) to bioethanol. *Afr. J. Biotechnol.* **2012**, *11*, 4921–4928.

(35) Quinzeni, I.; Capsoni, D.; Berbenni, V.; Mustarelli, P.; Sturini, M.; Bini, M. Stability of low-temperature $Li_7La_3Zr_2O_{12}$ cubic phase: The role of temperature and atmosphere. *Mater. Chem. Phys.* **2017**, *185*, 55–64.

(36) Asrofi, M.; Abral, H.; Kasim, A.; Pratoto, A. XRD and FTIR Studies of Nanocrystalline Cellulose from Water Hyacinth (Eichornia Crassipes) Fiber. *J. Metastable Nanocryst. Mater.* **2017**, *29*, 9–16.

(37) Tietz, F.; Wegener, T.; Gerhards, M. T.; Giarola, M.; Mariotto, G. Synthesis and Raman micro-spectroscopy investigation of $Li_7La_3Zr_2O_{12}$. *Solid State Ionics* **2013**, *230*, 77–82.

(38) Toda, S.; Ishiguro, K.; Shimonishi, Y.; Hirano, A.; Takeda, Y.; Yamamoto, O.; Imanishi, N. Low temperature cubic garnet-type CO_2-doped $Li_7La_3Zr_2O_{12}$. *Solid State Ionics* **2013**, *233*, 102–106.

(39) Galven, C.; Fourquet, J.-L.; Crosnier-Lopez, M.-P.; Berre, F. Instability of the Lithium Garnet $Li_7La_3Sn_2O_{12}$: Li+/H+ Exchange and Structural Study. *Chem. Mater.* **2011**, *23*, 1892–1900.

(40) Larraz, G.; Orera, G. A.; Sanjuán, M. L. Cubic phases of garnet-type $Li_7La_3Zr_2O_{12}$: the role of hydration. *J. Mater. Chem. A* **2013**, *1*, 11419–11428.

(41) Rosen, M.; Ye, R.; Mann, M.; Lobe, S.; Finsterbusch, M.; Guillon, O.; Fattakhova-Rohlfing, D. Controlling the lithium proton exchange of LLZO to enable reproducible processing and performance optimization. *J. Mater. Chem. A* **2021**, *9*, 4831–4840.

(42) Abraham, E.; Deepa, B.; Pothen, L. A.; Cintil, J.; Thomas, S.; John, M. J.; Anandjiwala, R.; Narine, S. S. Environmental friendly method for the extraction of coir fibre and isolation of nanofibre. *Carbohydr. Polym.* **2013**, *92*, 1477–1483.

(43) Chandra, J.; George, N.; Narayanankutty, S. K. Isolation and characterization of cellulose nanofibrils from arecanut husk fibre. *Carbohydr. Polym.* **2016**, *142*, 158–166.

(44) Nacos, M. K.; Katapodis, P.; Pappas, C.; Daferera, D.; Tarantilis, P. A. Kenaf xylan – A source of biologically active acidic oligosaccharides. *Carbohydr. Polym.* **2006**, *66*, 126–134.

(45) Pratibha, S.; Dhananjaya, N.; Pasha, A.; Khasim, S. Improved luminescence and LPG sensing properties of Sm^{3+}-doped lanthanum aluminate thin films. *Appl. Nanosci.* **2020**, *10*, 1927–1939.

(46) Mu, Q.; Wang, Y. Synthesis, characterization, shape-preserved transformation, and optical properties of La $(OH)_3$, $La_2O_2CO_3$, and La_2O_3 nanorods. *J. Alloys Compd.* **2011**, *509*, 396–401.

(47) Thangadurai, V.; Huggins, R. A.; Weppner, W. Use of simple ac technique to determine the ionic and electronic conductivities in pure and Fe-substituted SrSnO3 perovskite. *J. Power Source* **2002**, *108*, 64–69.

(48) Afyon, S.; Krumeich, F.; Rupp, J. L. M. A Shortcut to Garnet-type fast Li-ion conductors for all-solid state batteries. *J. Mater. Chem. A* **2015**, *3*, 18636–18648.

(49) Howard, M. A.; Clemens, O.; Kendrick, E.; Knight, K. S.; Apperley, D. C.; Anderson, P. A.; Slater, P. R. Effect of Ga incorporation on the structure and Li ion conductivity of $La_3Zr_2Li_7O_{12}$. *Dalton Trans.* **2012**, *41*, 12048–12053.

(50) Wu, J. F.; Chen, E. Y.; Yu, Y.; Liu, L.; Wu, Y.; Pang, W. K.; Peterson, V. K.; Guo, X. Gallium-doped LiLaZrO garnet-type electrolytes with high lithium-ion conductivity. *ACS Appl. Mater. Interfaces* **2017**, *9*, 1542–1552.

(51) Wolfenstine, J.; Ratchford, J.; Rangasamy, E.; Sakamoto, J.; Allen, J. L. Synthesis and high Li-ion conductivity of Ga-stabilized cubic $Li_7La_3Zr_2O_{12}$. *Mater. Chem. Phys.* **2012**, *134*, 571–575.

(52) Qin, S.; Zhu, X.; Jiang, Y.; Ling, M.; Hu, Z.; Zhu, J. Extremely dense microstructure and enhanced ionic conductivity in hot-isostatic pressing treated cubic garnet-type solid electrolyte of Ga2O3- doped Li7La3Zr2O12. *Funct. Mater. Lett.* **2018**, *11*, 1850029.

(53) Li, J.; Li, F.; Zhang, L.; Zhang, H.; Lassi, U.; Ji, X. Recent application of ionic liquids in quasi-solid-state lithium metal batteries. *Green Chem. Eng.* **2021**, *2*, 253–265.

(54) Pervez, A.; Kim, G.; Vinayan, B. P.; Cambez, M. A.; Kuenzel, M.; Hekmatfar, M.; Fichtner, M.; Passerini, S. Overcoming the Interfacial Limitations Imposed by the Solid-Solid Interface in Solid-State Batteries Using Ionic Liquid-Based Interlayers. *Small* **2020**, *16*, 2000279.

(55) Wu, B.; Wang, S.; Lochala, J.; Desrochers, D.; Liu, B.; Zhang, W.; Yang, J.; Xiao, J. The role of the solid electrolyte interphase layer in preventing Li dendritic growth in solid-state batteries. *Energy Environ. Sci.* **2018**, *11*, 1803–1810.

(56) Zhang, Z.; Zhang, L.; Liu, Y.; Wang, H.; Yu, C.; Zeng, H.; Wang, L.; Xu, B. Interface-Engineered $Li_7La_3Zr_2O_{12}$-Based Garnet Solid Electrolytes with supressed Li-Dendrite Formation and enhanced Electrochemical Performances. *ChemSusChem* **2018**, *11*, 3774–3782.

(57) Cao, D.; Sun, X.; Li, Q.; Natan, A.; Xiang, P.; Zhu, H. Lithium Dendrite in All-Solid-State Batteries: Growth Mechanism, Suppression Strategies, and characterizations. *Matter* **2020**, *3*, 57–94.